CrossMark

ORIGINAL PAPER: CHARACTERIZATION METHODS OF SOL-GEL AND HYBRID MATERIALS

Hydrothermal growth of undoped and boron doped ZnO nanorods as a photoelectrode for solar water splitting applications

Akash Sharma[1] · Mohua Chakraborty[1] · R. Thangavel[1] · G. Udayabhanu[2]

Abstract Undoped and boron-doped ZnO nanorods (NRs) were grown on ITO glass substrates by using hydrothermal techniques. The as grown nanorods were investigated by using X-ray diffraction (XRD), field emission scanning electron microscopy (FESEM), UV–visible spectroscopy, and photoelectrochemical study. XRD spectra reveal the confirmations regarding the hexagonal wurtzite structure along with preferential orientation (002). The observation of (002) peak shows a red shift. The average size distribution of NRs in doped and undoped sample ranges from 169 to 191 nm. The absorption spectra clearly revealed the band gap tunability feature of the samples with a change in doping percentage. Photoluminescence spectra clearly indicate the presence of oxygen defects. Photocurrent density as high as ~0.622 and 2.6 mA/cm^2 were obtained for undoped and 6% B-doped ZnO NRs arrays respectively, at +0.44 V vs. Ag/AgCl electrode under visible light AM 1.5 G (100 mW/cm^2) in 0.1 M electrolyte solutions of NaOH. More enhancement in photoconversion efficiency (PCE) from 0.491 to 2.054% was observed for undoped ZnO NRs and optimum 6% B-doped ZnO in 0.1 M NaOH electrolyte solution.

Graphical abstract
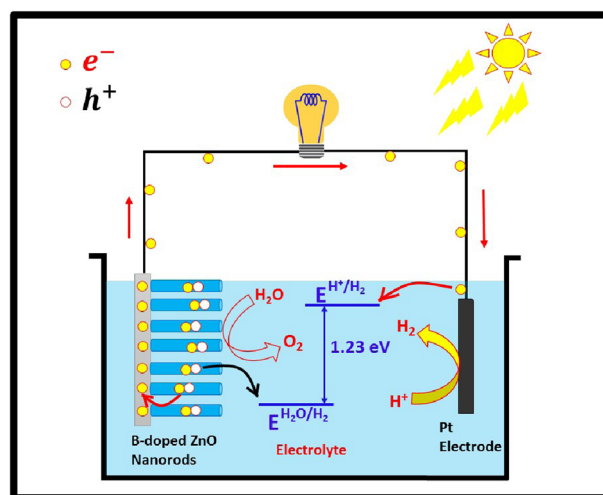
1 Introduction

The possibility to store solar energy in the form of chemical bonds such as hydrogen comes true via photoelectrochemical (PEC) water splitting. PEC cells have the ability to convert solar energy to consumable fuel by splitting water into hydrogen and oxygen. Generation of hydrogen by photo-induced electrolysis of water from a semiconductor/electrolyte interfaces is an efficient way for the production of clean energy. It has been realized as the

✉ R. Thangavel
    rtvel.res@gmail.com
    rthangavel@iitism.ac.in

1   Solar Energy Research Laboratory, Department of Applied Physics, Indian Institute of Technology (Indian School of Mines), Dhanbad 826004 Jharkhand, India

2   Department of Applied Chemistry, Indian Institute of Technology (Indian School of Mines), Dhanbad 826004 Jharkhand, India

most sustainable and clean method for hydrogen energy generation from abundant sunlight and water, because hydrogen on combustion produces water without leaving any remarkable harmful effect on the environment. Almost more than 200 compounds have been taken under trail for water splitting applications after the pioneer work of Fujishima and Honda [1], but the oxides like ZnO [2], TiO₂ [3], WO₃ [4], BiVO₄ [5], α-Fe₂O₃ [6] etc. still hold the major share in this field. Despite the best common features like their nontoxicity, stability, and inexpensive nature, still, they have limitations in efficiency due to structural defects, limited light absorptivity, low stability in aqueous solution, and short diffusion length [7].

ZnO is a well-known n-type material with many important properties like wide band gap (3.2 eV), direct band structure, large exciton binding energy of 60 meV at room temperature [8]. These properties of ZnO provide immense fidelity for its application as light emitting diode [9], sensors [10–12], thin film transistors [13]. Furthermore, it has been extensively used for conversion of solar energy into various product forms of energy because of its excellent electron mobility, electron transfer efficiency along with abundant morphologies, simple tailoring of nanostructures, and favourable environmental compatibility. Several investigations have been carried out on ZnO as a photoactive material for water splitting applications after it was first reported in 1969 for applications in dye-sensitized solar cells [14]. Its conduction band minimum lies at −0.31 V vs. normal hydrogen electrode (NHE) and valence band maxima at 2.89 V (vs. NHE), which makes it suitable for water oxidation (1.23 V vs. NHE) [15]. It has electron mobility higher of several order of magnitudes as compared with the most widely investigated oxide semiconductor, TiO₂ for water splitting applications [16]. Apart from that similar light dependence, better electron lifetime along with a lower recombination rate of ZnO has predicted it to be a better photoactive material than TiO₂ [17]. Despite of these excellent properties, ZnO has consistently shown reduced photoactivity due to the responsivity to ultraviolet light, which is mere 4% of the total solar spectrum; the fast recombination of photoinduced carriers, resulting in low photoconversion efficiency and photocorrosion in long-term processes, even in presence of sacrificial electrolyte [18].

For the improvement in photoelectrochemical performance and to overcome the material drawbacks of ZnO various modification has been done during synthesis. Enhancement of electrical as well as optical properties using suitable dopant is one of the feasible ways to improve the photoactivity [19]. The band gap engineering of ZnO, done by doping provides immense freedom in tuning the band gap, resulting in the improved optical properties. Group III elements such as B [20], Al [21], Ga [22], and In [23] have

been reported as a dopant for enhancement of the optical properties of ZnO, by several groups. Among all the group III elements, the lowest ionic radius (0.23 Å) and the highest electronegativity (2.04, Pauling Scale) of boron help in physical properties enhancement of host lattice ZnO [24].

The vertically aligned nanowires facilitate the efficient charge collection, separation, and transfer by providing a large interface area with the surrounding electrolyte medium. Therefore, these one-dimensional structures are very often being counted upon for photocatalytic efficiency enhancement. Enhanced photoelectrochemical properties can be achieved by the exposure of a maximum surface area of the semiconductor in the electrolyte solution. One-dimensional ZnO nanowire arrays can serve the purpose because of their large surface area-to-volume ratio. Various deposition techniques such as chemical vapor deposition [10, 25, 26], magnetron sputtering [27], pulsed laser deposition [28], electrodeposition [29], spray pyrolysis [30], and hydrothermal [31] have been adopted for the fabrication of ZnO nanorods. But hydrothermal method still catches the importance among all because of its simplicity, cost effectiveness, large area deposition, and flexibility in the compositional modification.

To date, numerous literature has been reported on ZnO NRs doped with several dopants. Yet there are very few reports on hydrothermally grown B-doped ZnO NRs [20, 32–34]. Herein, we have reported the enhancement of charge separation caused along with the addition of boron into ZnO NRs. In this report, a detail investigation on the effect on photoelectrochemical performance along with structural, optical, and electrical properties were carried out for B-doped ZnO NRs synthesized by a facile two-step method in ambient air conditions.

2 Experimental section

2.1 Materials

Zinc acetate dihydrate (Zn(CH₃COO)₂·2H₂O, 98% purity), Monoethanolamine (C₂H₇NO, 98% purity), Zinc nitrate hexahydrate (Zn(NO₃)₂·6H₂O, 98% purity), Hexamethylenetetramine (C₆H₁₂N₄, 99% purity) from Merck Chemicals; 2-Methoxyethanol, (C₃H₈O₂, 99% purity) and Trimethyl borate (C₃H₉BO₃, 99% purity) were purchased from Alfa Aesar Chemicals respectively and used as received without any further purification.

2.2 Synthesis

ZnO nanorod arrays were synthesized by sol–gel, spin coating and hydrothermal method through a two-step process; seed layer deposition and growth of nanorods as

reported earlier [35]. Figure 1 represents the schematic diagram of synthesis of undoped and doped ZnO NRs. Trimethyl borate, which served as a source of boron dopant was separately dissolved in de-ionized (DI) water as per the required concentration from 2.0 to 8.0 mol%. The boron precursor solution so obtained is finally added dropwise into the solution containing hexamethylenetetramine and zinc nitrate hexahydrate in desired concentration. For B-doped ZnO NR arrays all the growth conditions were kept similar as mentioned in our earlier report [35]. Finally, the prepared films were rinsed with DI water followed by drying at room temperature. The samples grown with several doping percentage i.e., 0, 2, 4, 6, and 8%; are hereafter named as ZnO, 2B_ZnO, 4B_ZnO, 6B_ZnO, 8B_ZnO, respectively.
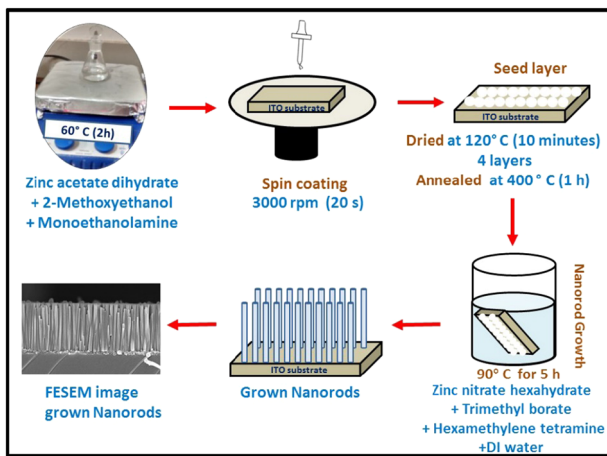
Fig. 1 A schematic demonstration of preparation of ZnO NRs and B-doped ZnO NRs with various doping concentration

2.3 Characterization techniques

The structural analysis of undoped and B-doped ZnO NRs was carried out via a PANalytical Empyrean X-Ray diffractometer using monochromatic CuK$_{\alpha 1}$ radiation ($\lambda = 1.5406$ Å).The surface morphologies of the nanostructured films were analyzed by using ZEISS Supra 55 field emission scanning electron microscopy (FESEM). The absorption spectra of the nanostructures were obtained using Agilent Cary 5000 UV–Vis-NIR double beam spectrophotometer. The optical absorption in the films deposited was determined by using a blank ITO substrate as reference. Photoluminescence spectroscopy was carried out using a Hitachi f-2500 spectrophotometer. The current–voltage measurements were performed by using a Keithley 2450 source meter. For photoelectrochemical measurement under light illumination, a three electrode cell configuration consist of a Pt wire, an Ag/AgCl (saturated with KCl) and grown thin films as counter, reference and working electrodes, respectively has been used. An aqueous solution of 0.1 M NaOH was used as electrolyte. The electrode potential was varied from −0.5 to 1.0 V using a potentiostat (Princeton EG & G Applied Research). The light and dark conditions were created using an Oriel AM 1.5 G filtered Xenon arc lamp with intensity set to 100 mW/cm^2.

3 Results and discussion

3.1 Structural properties

Figure 2 represents the X-ray diffraction (XRD) patterns of hydrothermally grown undoped and B-doped ZnO NRs.
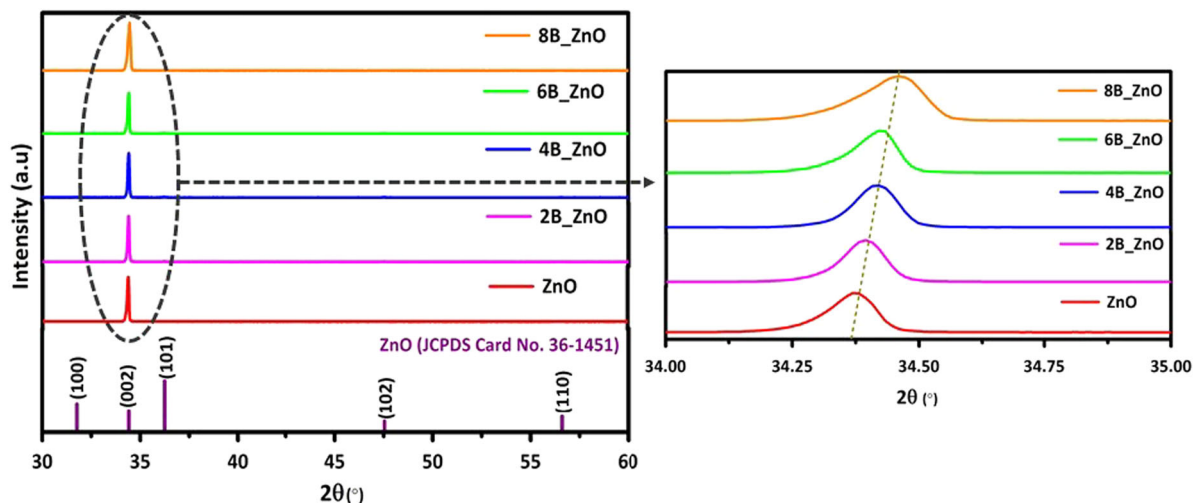
Fig. 2 XRD patterns of as-prepared ZnO NRs and B-doped ZnO NRs along with the magnified XRD pattern representing the higher angle shifting of (002) peak with increase in doping concentration

Table 1 The structural parameters, average diameter, approx. length, roughness calculated from XRD and FESEM characterization respectively

Sample	2θ at (002) plane (°)	c (Å)	Crystallite size (nm)	Stress σ (×10⁹) (N/m²)	Dislocation density (nm)⁻²	Average diameter (nm)	Approx length (μm)	Roughness
ZnO	34.374	5.214	85.92	0.757674	0.000135456	169	2.8	60.07352
2B_ZnO	34.394	5.211	95.85	0.498881	0.000108846	188	2.56	49.37349
4B_ZnO	34.417	5.207	95.46	0.208427	0.000109737	191	1.278	24.26103
6B_ZnO	34.425	5.206	90.07	0.104879	0.000123256	187	1.76	34.1258
8B_ZnO	34.458	5.201	63.36	−0.31647	0.000249102	189	2.6	49.87964

Crystallite size was calculated using Debye-Scherrer's formula

The characteristic diffraction peaks of the ZnO NRs are clearly observed in the diffraction patterns. The peak positions for the undoped and boron doped ZnO nanorod samples are in a close conformity with JCPDS card no.36-1451, space group P6₃mc), verifying the hexagonal wurtzite ZnO structure of the samples [36]. No other secondary phase's peaks were observed in the XRD spectrum after doping boron, which indicates the single crystalline nature of the samples. The high-intensity diffraction peak is indicative of the fact that reflections from (002) plane in ZnO nanowires are stronger as compared with the other planes [37]. So it is in harmony that the crystal has growth along c-axis based on the strongest, characteristic (002) diffraction peak, which is also in suitable agreement with earlier reported literature [36, 38].The red shift occurred in the doped ZnO samples has been clearly observed and represented in Fig. 2. Due to the substitution of lower ionic radius B^{3+} (0.02 nm) in place of either O^{2-} (0.14 nm) and/or, Zn^{2+} (0.074 nm) in ZnO host lattice, the crystal plane spacing shrinks resulting in the shifting of (002) peak towards higher angle [34]. The average crystallite size was calculated using the Debye-Scherrer's formula

$$D = \frac{0.9\,\lambda}{\beta \cos\theta} \tag{1}$$

$$\delta = \frac{1}{D^2} \tag{2}$$

The dislocation density can be estimated from the equation (2).

The lattice constants were calculated using the equation as follows,

$$\sin^2\theta = \left(\frac{\lambda^2}{4a^2}\right)\left[\frac{4}{3}\left(h^2 + hk + k^2\right) + \frac{l^2 a^2}{c^2}\right], \tag{3}$$

where λ is the wavelength of $CuK_{\alpha 1}$ radiation used (=1.5406 Å), and θ is the angle of diffraction. The stress induced in the ZnO matrix by the incorporation of B^{3+} ion can be estimated using the formula given in Eq. 4 and

represented in Table 1.

$$\sigma\left(\frac{N}{m^2}\right) = -453.6 \times 10^9 \left\{\frac{C_0 - C}{C_0}\right\}, \tag{4}$$

Where C is the lattice constant obtained from the (002) diffraction peak and C_0 is 5.205 Å for bulk ZnO. The induced stress effect changed the preferential orientation of the growing ZnO nanorods with an increase in the doping concentration of boron.

3.2 Surface morphology study

Figure 3 (a–e) represents the top view of the field emission scanning electron microscopy (FESEM) images of undoped and B-doped ZnO NRs. The samples were observed to be well contained with vertically aligned hexagonal nanorods in a regular manner on the substrate. The effect of boron concentration on the morphology can be clearly visualized in the cross-sectional images (inset of Fig. 3 (a–e)). The change of smoothly grown, uniformly distributed ZnO nanorods to unevenly distributed morphology indicates the consequence of boron doping into ZnO host matrix. All the FESEM images were analyzed using ImageJ software. The average nanorod lengths with increasing doping concentration were found to be of 2.8, 2.56, 1.278, 1.76, and 2.6 μm for ZnO, 2B_ZnO, 4B_ZnO, 6B_ZnO, and 8B_ZnO, respectively. Interestingly, all the grown NRs were found to be shorter than the undoped ZnO NRs with an increase in B concentrations. The growth mechanism of ZnO nanostructures can be explained by three steps namely: first, deposition of ZnO crystal seeds on the substrate; second growth of randomly oriented crystals from the seeds; and third, the growth of aligned nanorods after extended reactions resulting in the reduction of growth units [39, 40]. In a typical chemical process the growth of ZnO NRs are caused due to hydrolysis of zinc nitrate and $Zn(OH)_4^{2-}$ acts as the growth unit [41]. The dopant source as a boron precursor was introduced into the reaction path. The trivalent boron ion in the growth solution leads towards a decrease in the concentration of Zn^{2+} interstitial ions to
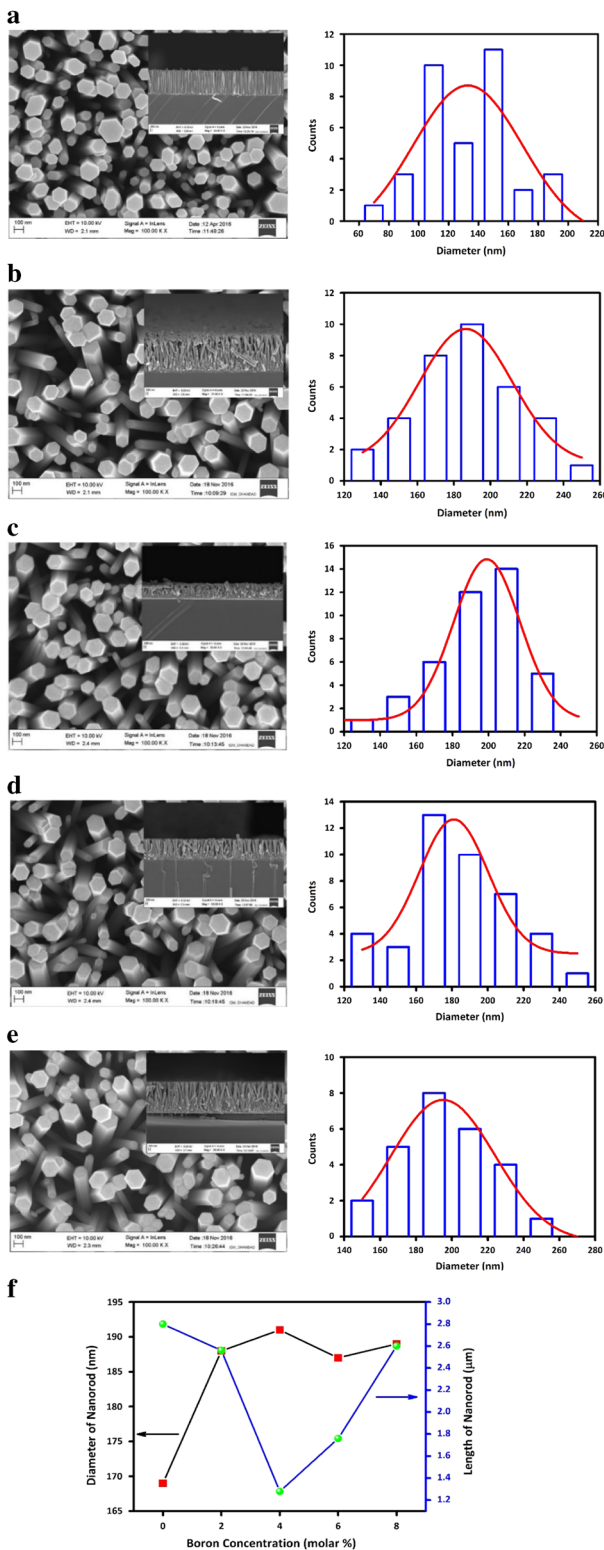
Fig. 3 FESEM images of top view of (**a**) undoped ZnO NRs, (**b**) 2B_ZnO, (**c**) 4B_ZnO, (**d**) 6B_ZnO, (**e**) 8B_ZnO along with the graphs representing distribution of diameters of samples respectively, (**f**) represents the variation in nanorod length and diameter distribution as a function of boron concentration. The inset (**a–e**) shows the cross-sectional view of the respective samples

compensate for the difference in the charge of the B-doped host lattice, [42] suppressing the growth of ZnO nanorod. On the other hand the NRs doped after 4% B shows an increase in the nanorods length, which indicate that the ZnO lattice had been doped with interstitial B^{3+} ions and/or that Zn^{2+} ion in the lattice had been substituted with the higher valence B^{3+} ions, which in turn increased the length of the nanorods [21]. The average diameter of the nanorods has also varies as 169, 188, 191, 187, and 189 nm with increased doping concentration ranging from 0 to 8% (shown in Fig. 3 (f)). Roughness factor was estimated from the hexagonally packed model as reported earlier by Kim et al. and summarized in Table 1 [43].

3.3 Optical properties

Light absorption in the visible region is one of the essential key features for photocatalytic materials. The Ultraviolet−Visible (UV−Vis) absorption spectra powerfully reveal a clear understanding and developing the band structure and an energy gap E_g of crystalline structure. Figure 4 represents the absorption spectra of hydrothermally grown undoped and B-doped ZnO NRs recorded within the spectral range 350–750 nm. The band gap values were estimated from the absorption spectra by using the Tauc's relation [44]. The calculated values of band gap for all the samples are summarized in the Table 2.

The absorption band edge for undoped ZnO NRs was obtained at ~394 nm. It has lower absorption edge in the visible light range. The band gap tunability after doping can be understood as the replacement of Zn^{2+} ion by B^{3+} ion. With B-doping up to 6%, a decrement in the band gap values of ZnO NRs was observed from 3.25 to 3.13 eV,
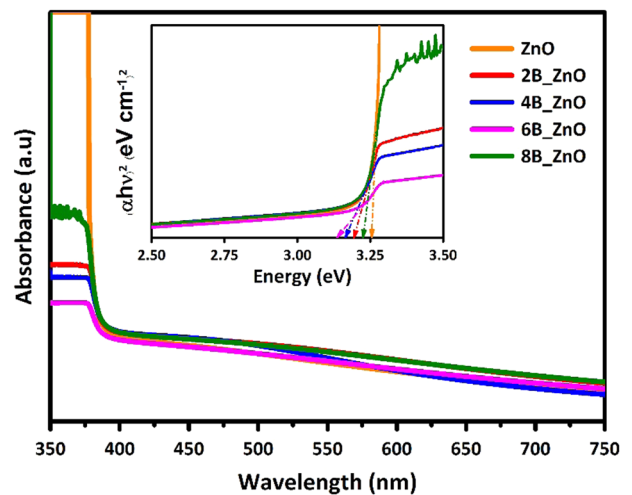

Fig. 4 UV−Vis absorption spectra (inset shows Tauc's plots.) of ZnO NRs and B-doped ZnO NRs with various doping concentration

Table 2 The optical band gap, absolute electronegativity and conduction band and valence band level estimated theoretically from absorption spectrum results

Sample	Optical band gap (eV)	Absolute electronegativity (χ)	CB level (eV)	VB level (eV)
ZnO	3.25	5.79249	−0.332505	2.91749
2B_ZnO	3.19	5.79037	−0.304625	2.88537
4B_ZnO	3.16	5.78825	−0.291745	2.86825
6B_ZnO	3.13	5.78613	−0.2778864	2.85113
8B_ZnO	3.22	5.78402	−0.325982	2.89402

whereas, for 8B_ZnO sample, the band gap value increases to 3.22 eV in comparison with ZnO NRs. The conduction band and valence band levels were calculated theoretically and represented in Table 2 in a similar way as reported earlier [45, 46]. The reduction of band gap with an increase in B concentration can be attributed to the new ion (B^{3+}) energy level formed within the valence band and conduction band. The blue shift further observed with 8B_ZnO can be explained by Burstein-Moss (BM) effect. According to BM effect, the fermi level lying below the conduction band of an intrinsic semiconductor gets shifted above it due to increase in the carrier concentration and hence causes a blue shift of band gap. The increment in carrier concentration is clearly indicated by the interstitial zinc atoms or oxygen vacancies at room temperature [47].

Photoluminescence (PL) spectroscopy is an essential tool for explaining the transfer and recombination process of the photogenerated electron-hole pairs in the semiconductor. The presence of different type of structural defects such as zinc and oxygen interstitials and/or vacancies in ZnO nanostructure results in different radiative recombination transitions between electrons either from the conduction band or trapping levels and photo generated or trapped holes can be studied from PL measurement [48]. Figure 5 represents the room temperature PL spectra of B-doped ZnO NRs samples as a function of boron concentration with excitation at a wavelength of 320 nm. The PL spectra of ZnO consists of the UV emission caused due to excitonic recombination which is in harmony with the near band edge (NBE) emission of ZnO, while the deep level emissions (DLE) in the visible spectral region results from their combination of photo-generated holes with various structural defects e.g., ionized charge states of intrinsic defects, oxygen vacancies, Zn interstitials, zinc vacancies, and oxygen antisites [49]. From the PL spectra the UV emission peaks at 379, 396 nm, a violet-blue band at 452 nm, a strong blue band at 470 nm, a greenish blue emission at 484 nm, a weak blue–green emission at 492 nm, and a broad peak ranging from 500 to 650 nm can be clearly observed. The 379 nm peak in the UV emission identifies the typical exciton emission or NBE from
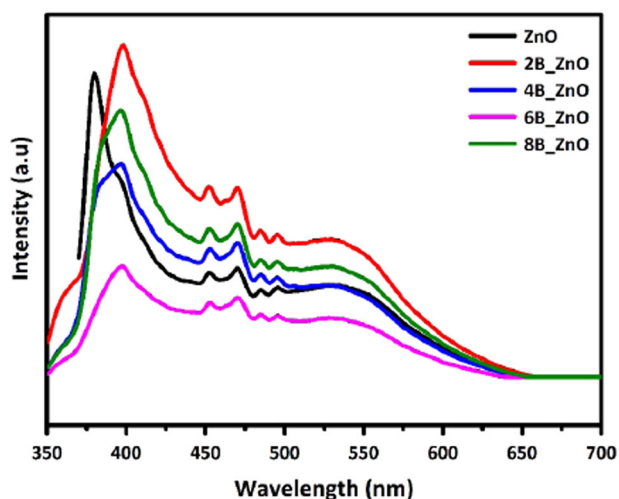

Fig. 5 The photoluminescence spectra of undoped and B-doped ZnO NRs films

the recombination of free excitons [50]. The peak at 396 nm is attributed to the surface states (V_{Zn}) or band tail states in ZnO [51]. The range of wavelength 450–650 nm DLE region is usually observed due to the optical centers associated with impurities such as native defects [52]. The surface defects in ZnO NRs are the main cause for the weak blue emissions [53]. The strong blue band at 470 nm has been resulted due to the electron transitions from the interstitial Zn_i to the intrinsic defect V_{Zn}.

Furthermore, a green emission can be clearly observed at ~543 nm, which is referred to as the DLE and often attributed to singly ionized oxygen vacancies (V_O^+) [54]. Figure 5 clearly indicates that with an increase in doping percentage of B in the hydrothermal solution the PL intensity has been decreased and at 6% B-doping it has attended the minimum value. This can be inferred that B^{3+} ion has been successfully incorporated into the ZnO host matrix. But after that in the case of 8B_ZnO again PL intensity has been increased, which indicates the enhanced recombination effect [55, 56]. As observed clearly from the PL graph the weak green emission, the 6B_ZnO sample exhibited the lowest surface defect [35]. The lesser defect causes the reduction in recombination centers for photoelectrons and holes by acting like an energy barrier at the interface, promoting the charge separation and hence improving the PEC performances. To investigate the impact of the oxygen vacancy on photoelectrochemical properties further PEC performance was analyzed using a three electrode system.

3.4 Electrical properties

Figure 6 represents the current–voltage (I–V) characteristic graph for all the grown nanorods, measured both under dark
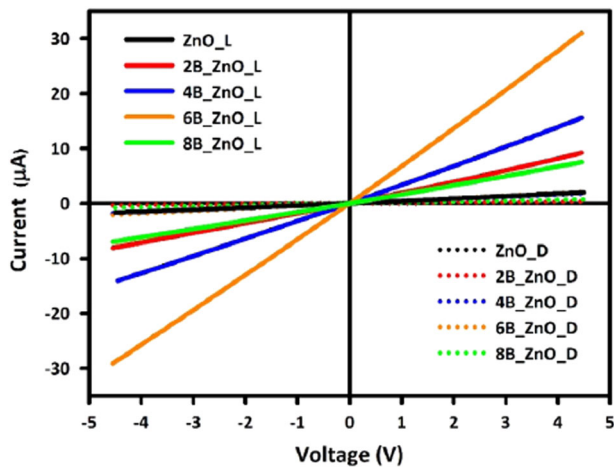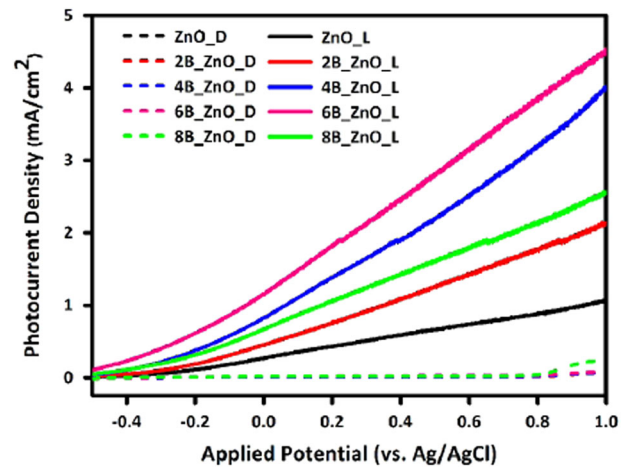
Fig. 6 Current vs. voltage measurements of undoped ZnO NRs and B-doped ZnO NRs films under dark and UV illumination condition

Fig. 7 Photocurrent density (mA/cm^2) vs. Applied Potential (vs. Ag/AgCl) measurements of undoped ZnO NRs and B-doped ZnO NRs films under dark and visible light illumination at room temperature in 0.1 M NaOH electrolyte solution

and illumination conditions in the ambient atmosphere within a voltage range from −4.5 to +4.5 V. The linear graphs clearly shows the ohmic nature of the samples. Further with an increase in the doping concentration of B, a remarkable increase in the current values has been observed. The sample 6B_ZnO exhibits the highest current value of ~31 μA among all the synthesized samples under UV illumination at the voltage +4.5 V. The enhancement in photocurrent values can be understood in the following manner. Upon UV illumination, electrons at the top of the valence band start absorbing the requisite amount of photon energy and jumps to the conduction band. As a result, photoinduced carriers, i.e., holes in the valence band and electrons in the conduction band are created in the ZnO nanostructure. The substitution of B^{3+} ion in sites of Zn^{2+} creates more electrons in the ZnO matrix [57]. With the increase in doping concentration of trivalent B^{3+} ion, more number of carriers are generated in the nanorod arrays; thus helping more number of electrons to reach the conduction band of B-doped ZnO [58]. But surprisingly increasing the doping percentage up to an extent i.e., for 8B_ZnO sample, the photocurrent value has been reduced. It can be accounted for the decrease in grain size and increasing number of grain boundaries, which finally contributes to the charge carrier scattering mechanism [59]. The enhancement of photocurrent upon illumination have been estimated using the same method as reported in earlier literature and summarized in Table 2 [60].

3.5 Photoelectrochemical (PEC) properties

In order to explore the electrochemical behavior of various samples, a three electrode PEC cell was used by ZnO NRs and various B-doped ZnO photoelectrodes. The dark and photoresponse of these electrodes have been evaluated in a
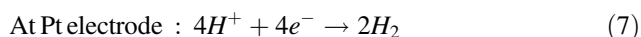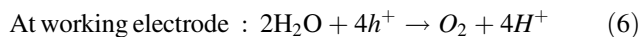
PEC cell and the performance has been shown in Fig. 7. The photoactivity of each photoanode was determined by measuring the photocurrent density generated, while the electrode was irradiated from the front (semiconductor to substrate) side of the film while being immersed in electrolyte solutions. The dark current density for undoped ZnO NRs has been observed in the order of 0.004 mA/cm^2, while under front illumination a photocurrent density value of ~0.622 mA/cm^2 was obtained in 0.1 M NaOH at 0.44 V (vs. Ag/AgCl). Pronounced photoresponse under illumination was observed with the subsequent increase in dopant concentration. But interestingly a decrease in the photocurrent density value for the 8B_ZnO film has been observed. The 6B_ZnO photoelectrode exhibit highest photocurrent density of ~2.6 mA/cm^2 in 0.1 M NaOH (at +0.44 V vs. Ag/AgCl) electrolyte solution which is more than 318, 123, 30, and 74% enhancement compared to the undoped ZnO (0.622 mA/cm^2), 2B_ZnO (1.162 mA/cm^2), 4B_ZnO (2 mA/cm^2), 8B_ZnO (1.492 mA/cm^2) samples, respectively. Among all the prepared films the 6B_ZnO sample was superior in PEC properties along with the immediate photocurrent generation at lower potential values, which indicates the dominance of fast charge transport over the electron–hole recombination. The remarkable increment in photocurrent values can be attributed not only to the increase in photo-absorption, which is in accordance with our optical results but also to the reduced surface defects caused due to the insertion of B in ZnO host matrix. This enhancement in photocurrent density revealed that the separation of photogenerated electron-hole pairs occurs more effectively after insertion of B in ZnO host matrix, which resulted in a decrease in the recombination probability [34]. But for the 8B_ZnO sample photocurrent density values has been decreased due to increase in surface

defects, which has been confirmed from the photo-luminescence results as well as for the increase in the band gap value. Although the above study indicates the quantitative discussions on overall photocurrent production, still further investigations are required to understand the carrier path as well as to check their applicability in nanostructured systems.

Initially, if a semiconductor is placed within an electrolyte solution, flow of electric current occurs across the junction until the chemical potential are equalized and an electronically balanced condition is created, i.e., the Fermi energy of the electrons in the semiconductor gets balanced with the redox potential of the electrolyte. As the applied potential values have been increased to more positive values, the photocurrent increased towards more positive values, which is regarded to be anodic. So B-doped ZnO can be considered to be an n-type semiconductor (n-SC). When the system is illuminated, a photon is absorbed by one nanocrystal, thus generating an electron/hole pair due to the initial events of direct recombination and separation. After the pair formation, in order to get the either of the charges separated one of the charge carrier must be transferred to the electrolyte much faster than the other. This can be achieved easily by using liquid junctions, as the holes travel faster in the electrolyte medium causing reduction of the recombination rate between electrons and holes [61]. Here, in an n-SC, holes being present in the valence band, preferentially gets injected into the electrolyte and are captured by the electrons from water oxidation (Eq. 6). Meanwhile, the conduction band electron reaches the conducting side of the substrate after passing several crystallites. The negative charge carriers move to the current collector through the external circuit, reaching the counter electrode and causing reduction of the water with the application of suitable potential (Eq. 7). Thus an anodic photocurrent is generated as shown in Fig 7. The process is governed by the following two chemical equations at the electrodes surfaces:

$$At\ working\ electrode\ :\ 2H_2O + 4h^+ \rightarrow O_2 + 4H^+ \qquad (6)$$

$$At\ Pt\ electrode\ :\ 4H^+ + 4e^- \rightarrow 2H_2 \qquad (7)$$

Hence the overall PEC reaction for the n-SC photoelectrodes can be represented by the following equation [62]

$$4h\nu + (n-SC) + 2H_2O \rightarrow 2H_2 + O_2 + (n-SC) \qquad (8)$$
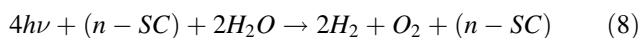
Whenever external voltage is applied to an n-SC in contact with an electrolyte in absence of space charge layer in the semiconductor, the conduction band and valence band are flat at the semiconductor-electrolyte interface and the applied potential is equal to E_{fb}, the flat band potential [63]. At this potential no electron-hole pairs are generated and hence the current flow stops across the semiconductor.
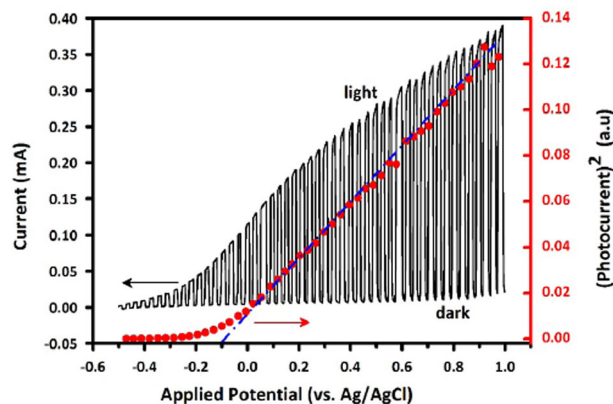
Fig. 8 Flat band potential (E_{fb}) measurement of the optimized 6B_ZnO film in aqueous electrolyte, 0.1 M NaOH: black line corresponds to current as a function of Applied potential (vs. Ag/AgCl) and red line indicates the square of the photocurrent plotted against the potential to extrapolate the value of E_{fb}
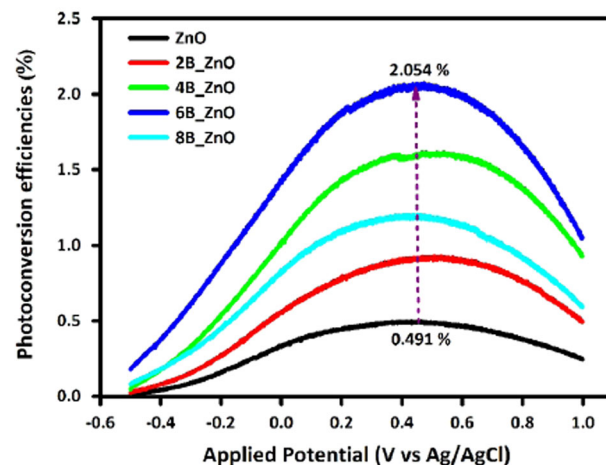
Fig. 9 PCE (%) for undoped ZnO NRs and B-doped ZnO NRs films under dark and visible light illumination at room temperature using 0.1 M NaOH as an electrolyte solution

Again with increase in applied bias along positive axis shifts the Fermi level towards more negative values of energy (in solid state vacuum scale) and the band bends upward. In dark condition, this establishes a barrier to charge transfer and current flow stops. The flat band potential value thus can be calculated by using Butler method according to the following equation [63, 64].

$$i_{ph}^2 \approx (E - E_{fb}) \qquad (9)$$

Where i_{ph} represents the photocurrent and E is the applied potential bias. According to this equation the intercept of the linear region of the i_{ph}^2 vs. E plot with abscissa will be E_{fb}. Using the above equation the flat band potential was determined to be -0.1 V (vs. Ag/AgCl) for the optimized sample 6B_ZnO as shown in the Fig. 8.

Table 3 Photocurrent and photocurrent density values along with enhancement percentage (δ%) due to illumination from I-V and LSV measurements. Photoconversion efficiency of B-doped ZnO nanorods

Sample	Photocurrent (μA) values at +4.5 V from I–V curve			Photocurrent density (mA/cm^2) at +0.44 V from LSV curve			PCE (%)
	Dark (I_D)	Illumination (I_L)	$\delta(\%)$	Dark (J_D)	Illumination (J_L)	$\delta(\%)$	
ZnO	0.138	1.99	1457.78	0.00394	0.622	318	0.491
2B_ZnO	0.339	9.21	236.59	0.00649	1.162	123	0.918
4B_ZnO	1.77	15.6	98.72	0.00866	2.0	30	1.580
6B_ZnO	2.08	31.0	–	0.0241	2.6	–	2.054
8B_ZnO	0.727	7.5	313.33	0.0201	1.492	74	1.178

The solar energy to chemical energy conversion efficiency, also named as photoconversion efficiency (PCE) (η) for PEC water splitting of photoanodes was estimated by using the equation below [65]

$$\eta(\%) = \frac{\text{total power output} - \text{electrical input}}{\text{light power input}} \times 100$$

$$= \frac{J_p \left[1.23 - V_{\text{app}} \right]}{P_{\text{light}}} \times 100 \qquad (10)$$

where V_{app} (in volts) is the applied external potential versus reversible hydrogen electrode (RHE), J_p is the externally measured current density (mA cm^{-2}) at V_{app} and P_{light} is the power density of the incident light (mW cm^{-2}). Figure 9 shows the PCE of the B-doped ZnO NRs arrays films with variation in molar concentrations and the curve for ZnO was plotted for reference. The PCE values estimated for all the samples were represented in Table 3. Significant increase was observed after B doping on ZnO NRs and for 6B_ZnO sample maximum PCE of 2.054% was observed, which is approximately 4 times as compared to undoped ZnO NRs film electrode. Increasing the concentration further the efficiency decreases, which is consistent with the photocurrent results. Moreover this indicates, the suitable modification in the electronic states of the sample has been occurred, hence making B-doped ZnO a potential candidate for photoelectrochemical cell.

4 Conclusion

In summary, B-doped ZnO NRs were synthesized by using low cost facile sol–gel hydrothermal technique. Along with variation in doping concentration, the hexagonal structure has been maintained for all the grown NRs as revealed by XRD and FESEM images. Using boron as a dopant shows an increase in carriers in the ZnO matrix, thus helping more number of electrons to reach the conduction band, resulting in an enhancement of the photocurrent values. The highest photocurrent observed from the I–V graph for the 6B_ZnO sample was ~14 times enhanced as compared to the undoped ZnO NRs. It indicates that with suitable selection

of dopant concentration the conductivity has been increased promoting higher photocurrent values. Furthermore, photoelectrochemical performance of the samples provided an insight into their use as photoelectrodes for PEC solar cell. The anodic photocurrent observed for the B-doped ZnO NRs claims their n-type nature. The 6B_ZnO photoelectrode exhibited highest photocurrent density of ~2.6 mA/cm^2, which was nearly 318% enhancement as compared with its undoped counterpart. It indicated that efficient charge separation has occurred as well as the recombination probability also decreased after doping boron in ZnO host matrix. Based on the above notable facts the B-doped ZnO NRs can be used in photoelectrochemical cells to serve better as photoelectrodes due to their superior photoinduced properties over ZnO NRs. By choosing suitable doping concentration along with proper electrolyte, the B-doped ZnO NRs arrays can be promoted for applications in the photoelectrochemical solar cell.

Compliance with ethical standards

Conflict of interest The authors declare that they have no competing interests.

References

1. Fujishima A, Honda K (1972) TiO$_2$ photoelectrochemistry and photocatalysis. Nature 213:8656
2. Fan J, Güell F, Fábrega C, Shavel A, Carrete A, Andreu T, Ramón Morante J, Cabot A (2011) Enhancement of the photoelectrochemical properties of Cl-doped ZnO nanowires by tuning their coaxial doping profile. Appl Phys Lett 99:262102

3. Zhang Z, Yuan Y, Liang L, Cheng Y, Shi G, Jin L (2008) Preparation and photoelectrocatalytic activity of ZnO nanorods embedded in highly ordered TiO_2 nanotube arrays electrode for azo dye degradation. J Hazard Mater 158:517–522

4. Lin J, Hu P, Zhang Y, Fan M, He Z, Ngaw CK, Loo JSC, Liao D, Tan TTY (2013) Understanding the photoelectrochemical properties of a reduced graphene oxide–WO_3 heterojunction photoanode for efficient solar-light-driven overall water splitting. RSC Adv 3:9330–9336

5. Yengantiwar A, Palanivel S, Archana PS, Ma Y, Pan S, Gupta A (2017) Direct liquid injection chemical vapor deposition of molybdenum-doped bismuth vanadate photoelectrodes for efficient solar water splitting. J Phys Chem C 121:5914–5924

6. Chakraborty M, Roy D, Biswas A, Thangavel R, Udayabhanu G (2016) Structural, optical and photo-electrochemical properties of hydrothermally grown ZnO nanorods arrays covered with α-Fe_2O_3 nanoparticles. RSC Adv 6:75063–75072

7. Mayer MT, Lin Y, Yuan G, Wang D (2013) Forming heterojunctions at the nanoscale for improved photoelectrochemical water splitting by semiconductor materials: case studies on hematite. Acc Chem Res 46:1558–1566

8. Norton DP (2004) Synthesis and properties of epitaxial electronic oxide thin-film materials. Mater Sci Eng R Rep 43:139–247

9. Nadarajah A, Word RC, Meiss J, Konenkamp R (2008) Flexible inorganic nanowire light-emitting diode. Nano Lett 8:534–537

10. Lupan O, Chow L, Chai G (2009) A single ZnO tetrapod-based sensor. Sens Actuat B Chem 141:511–517

11. Kim J, Park W, Lee C (2006) ZnO nanorod biosensor for highly sensitive detection of specific protein binding. J Korean Phys Soc 49:1635–1639

12. Tien LC, Sadik PW, Norton DP, Voss LF, Pearton SJ, Wang HT, Kang BS, Ren F, Jun J, Lin J (2005) Hydrogen sensing at room temperature with Pt-coated ZnO thin films and nanorods. Appl Phys Lett 87:1–3

13. Hong W-K, Sohn JI, Hwang D-K, Kwon S-S, Jo G, Song S, Kim S-M, Ko H-J, Park S-J, Welland ME, Lee T (2008) Tunable electronic transport characteristics of surface-architecture-controlled ZnO nanowire field effect transistors. Nano Lett 8:950–956

14. Tributsch H, Gerischer H (1969) The use of semiconductor electrodes in the study of photochemical reactions. Berichte der Bunsengesellschaft für Phys Chemie 73:850–854

15. Grätzel M (2001) Photoelectrochemical cells. Nature 414:338–344

16. Chandiran AK, Abdi-Jalebi M, Nazeeruddin MK, Grätzel M (2014) Analysis of electron transfer properties of ZnO and TiO_2 photoanodes for dye-sensitized solar cells. ACS Nano 8:2261–2268

17. Chou TP, Zhang Q, Cao G (2007) Effects of dye loading conditions on the energy conversion efficiency of ZnO and TiO_2 dye-sensitized solar cells. J Phys Chem C 111:18804–18811

18. Wang Y, Zheng YZ, Lu S, Tao X, Che Y, Chen JF (2015) Visible-light-responsive TiO_2 coated ZnO:I nanorod array films with enhanced photoelectrochemical and photocatalytic performance. ACS Appl Mater Interfaces 7:6093–6101

19. Archana PS, Shan Z, Pan S, Gupta A (2016) Photocatalytic water oxidation at bismuth vanadate thin film electrodes grown by direct liquid injection chemical vapor deposition method. Int J Hydrog Energy 42:8475–8485

20. Yu Q, Li J, Li H, Wang Q, Cheng S, Li L (2012) Fabrication, structure, and photocatalytic activities of boron-doped ZnO nanorods hydrothermally grown on CVD diamond film. Chem Phys Lett 539–540:74–78

21. Kim S, Kim MS, Nam G, Leem J-Y (2012) Structural and blue emission properties of Al-doped ZnO nanorod array thin films grown by hydrothermal method. Electron Mater Lett 8:445–450

22. Zhu L, Li J, Ye Z, He H, Chen X, Zhao B (2008) Photoluminescence of Ga-doped ZnO nanorods prepared by chemical vapor deposition. Opt Mater 31:237–240

23. Fang TH, Kang SH (2010) Optical and physical characteristics of In-doped ZnO nanorods. Curr Appl Phys 10:1076–1086

24. Tahar RBH, Tahar NBH (2005) Boron-doped zinc oxide thin films prepared by sol–gel technique. J Mater Sci 40:5285–5289

25. Liu X, Wu X, Cao H, Chang RPH (2004) Growth mechanism and properties of ZnO nanorods synthesized by plasma-enhanced chemical vapor deposition. J Appl Phys 95:3141–3147

26. Park WI, Kim DH, Jung SW, Yi GC (2002) Metalorganic vapor-phase epitaxial growth of vertically well-aligned ZnO nanorods. Appl Phys Lett 80:4232–4234

27. Liang L, Huang Z, Cai L, Chen W, Wang B, Chen K, Bai H, Tian Q, Fan B (2014) Magnetron sputtered zinc oxide nanorods as thickness-insensitive cathode inter layer for perovskite planar-heterojunction solar cells. ACS Appl Mater Interfaces 6:20585–20589

28. Djurišić AB, Leung YH, Tam KH, Ding L, Ge WK, Chen HY and Gwo S (2006) Green, yellow, and orange defect emission from ZnO nanostructures: influence of excitation wavelength. Appl Phys Lett 88:103107

29. Kim H, Moon J, Lee H (2009) Growth of ZnO nanorods on various substrates by electrodeposition. Electron Mater Lett 5:135–138

30. Maldonado A, Asomoza R, Cañetas-Ortega J, Zironi E, Hernández R, Patiño R, Solorza-Feria O (1999) Effect of the pH on the physical properties of ZnO:In thin films deposited by spray pyrolysis. Sol Energy Mater Sol Cells 57:331–344

31. Yang H, Song Y, Li L, Ma J, Chen D, Mai S, Zhao H (2008) Large-scale growth of highly oriented ZnO nanorod arrays in the Zn-NH_3·H_2O hydrothermal system. Cryst Growth Des 8:1039–1043

32. Tsin F, Thomere A, Bris ALe, Collin S, Lincot D, Rousset J (2016) Influence of a boron precursor on the growth and optoelectronic properties of electrodeposited zinc oxide thin film. ACS Appl Mater Interfaces 8:12298–12306

33. Rahman MYA, Roza L, Umar AA, Salleh MM (2016) Effect of dimethyl borate composition on the performance of boron doped ZnO dye-sensitized solar cell (DSSC). J Mater Sci Mater Electron 27:2228–2234

34. Wang W, Ai T, Yu Q (2017) Electrical and photocatalytic properties of boron-doped ZnO nanostructure grown on PET–ITO flexible substrates by hydrothermal method. Sci Rep 7:1–11

35. Thangavel R, Chang Y-C (2012) Investigations on structural, optical and electrical properties of p-type ZnO nanorods using hydrothermal method. Thin Solid Films 520:2589–2593

36. Bu IYY, Yeh Y-M (2012) Effects of sulfidation on the optoelectronic properties of hydrothermally synthesized ZnO nanowires. Ceram Int 38:3869–3873

37. Chen HM, Chen CK, Liu R-S, Wu C-C, Chang W-S, Chen K-H, Chan T-S, Lee J-F, Tsai DP (2011) A new approach to solar hydrogen production: a ZnO–ZnS solid solution nanowire array photoanode. Adv Energy Mater 1:742–747

38. Guo P, Jiang J, Shen S, Guo L (2013) ZnS/ZnO heterojunction as photoelectrode: type II band alignment towards enhanced photoelectrochemical performance. Int J Hydrog Energy 38:13097–13103

39. Tian ZR, Voigt J, Liu J, McKenzie B, McDermott MJ, Rodriguez M, Konishi H, Xu H (2003) Complex and oriented ZnO nanostructures. Nat Mater 2:821–826

40. Das R, Kumar A, Kumar Y et al. (2015) Effect of growth temperature on the optical properties of ZnO nanostructures grown by simple hydrothermal method. RSC Adv 5:60365–60372

41. Aslan F, Tumbul A, Go A, Budakog R, Mutlu IH (2016) Growth of ZnO nanorod arrays by one-step sol–gel process. J Sol–Gel Sci Technol 80:389–395

42. Hosono E, Fujihara S, Kimura T (2004) Synthesis, structure and photoelectrochemical performance of micro/nano-textured ZnO/eosin Y electrodes. Electrochim Acta 49:2287–2293

43. Kim H, Lee J, Yantara N, Boix PP, Kulkarni S, Mhaisalkar S, Grätzel M, Park N (2013) high efficiency solid-state sensitized solar cell-based on submicrometer rutile TiO_2 nanorod and CH_3NH_3 PbI_3 perovskite sensitizer. Nano Lett 13:2412–2417

44. Chakraborty M, Thangavel R, Biswas A, Udayabhanu G (2016) Facile synthesis, and the optical and electrical properties of nanocrystalline $ZnFe_2O_4$ thin films. CrystEngComm 18:3095–3103

45. Pearson RG (1988) Absolute electronegativity and hardness: application to inorganic chemistry. Inorg Chem 27:734–740

46. Lee G-J, Anandan S, Masten SJ, Wu JJ (2016) Photocatalytic hydrogen evolution from water splitting using Cu doped ZnS microspheres under visible light irradiation. Renew Energy 89:18–26

47. Banu Bahşi Z, Oral AY (2007) Effects of Mn and Cu doping on the microstructures and optical properties of sol–gel derived ZnO thin films. Opt Mater 29:672–678

48. Othman AA, Ali MA, Ibrahim EMM, Osman MA (2016) Influence of Cu doping on structural, morphological, photoluminescence, and electrical properties of ZnO nanostructures synthesized by ice-bath assisted sonochemical method. J Alloys Compd 683:399–411

49. Das D, Mondal P (2014) Photoluminescence phenomena prevailing in c-axis oriented intrinsic ZnO thin films prepared by RF magnetron sputtering. RSC Adv 4:35735–35743

50. Xia CH, Hu CG, Hu CH, Ping Z, Wang F (2011) Room-temperature ferromagnetic properties of Cu-doped ZnO rod arrays. Bull Mater Sci 34:1083–1087

51. Palni PP, Kumari S, Baruah NG, Singh DKGPK (2007) Effect of annealing on high quality zinc oxide nanowires synthesized by catalytic vapor-deposition. Nano Trends 3:1–6

52. Thapa D, Huso J, Morrison JL, Corolewski CD, McCluskey MD, Bergman L (2016) Achieving highly-enhanced UV photoluminescence and its origin in ZnO nanocrystalline films. Opt Mater 58:382–389

53. Wang J, Gao L (2004) Hydrothermal synthesis and photoluminescence properties of ZnO nanowires. Solid State Commun 132:269–271

54. Shi S, Xu J, Zhang X, Li L (2011) Effect of annealing on the structural and luminescent properties of ZnO nanorod arrays grown at low temperature. J Appl Phys 109:103508

55. Lin Y, Yuan G, Sheehan S, Zhou S, Wang D (2011) Hematite-based solar water splitting: challenges and opportunities. Energy Environ Sci 4:4862–4869

56. Sivula K, Le Formal F, Gratzel M (2011) Solar water splitting: progress using hematite (α-Fe_2O_3) photoelectrodes. ChemSusChem 4:432–449

57. Kim S, Park H, Nam G, Yoon H, Kim B, Ji I, Kim Y, Kim I, Park Y, Kang D, Leem JY (2014) Hydrothermally grown boron-doped ZnO nanorods for various applications: structural, optical, and electrical properties. Electron Mater Lett 10:81–87

58. Yun S, Lee J, Chung J, Lim S (2010) Improvement of ZnO nanorod-based dye-sensitized solar cell efficiency by Al-doping. J Phys Chem Solids 71:1724–1731

59. Bhattacharjee S, Sarkar PK, Roy A (2016) Polyvinyl-alcohol based devices with highly conductive, optically active boron-doped ZnO nanoparticles for efficient resistive-switching at ultralow operating voltage. Superlattices Microstruct 100:1057–1063

60. Chakraborty M, Ghosh A, Thangavel R, Asokan K (2016) Conduction mechanism in mesoporous hematite thin films using low temperature electrical measurements and theoretical electronic band structure calculations. J Alloys Compd 664:682–689

61. Hodes G (1992) Nanocrystalline photoelectrochemical cells. J Electrochem Soc 139:3136

62. Wolcott A, Smith WA, Kuykendall TR, Zhao Y, Zhang JZ (2009) Photoelectrochemical study of nanostructured ZnO thin films for hydrogen generation from water splitting. Adv Funct Mater 19:1849–1856

63. Natu G, Wu Y (2010) Photoelectrochemical study of the ilmenite polymorph of $CdSnO_3$ and its photoanodic application in dye-sensitized solar cells. J Phys Chem C 114:6802–6807

64. Butler MA (1977) Photoelectrolysis and physical properties of the semiconducting electrode WO_2. J Appl Phys 48:1914–1920

65. Khan SUM, Al-Shahry M, Ingler WB (2002) Efficient photochemical water splitting by a chemically modified n-TiO_2. Science 297:2243–2245